RSC Advances

PAPER

View Article Online
View Journal | View Issue

Cite this: *RSC Adv.*, 2021, **11**, 5044

Design of ZIF-based hybrid nanoparticles with hyaluronic acid-augmented ROS behavior for dual-modality PA/NIR-II FL imaging†

Botao Qu, ‡[a] Yahong Han,‡[ab] Juan Li,[a] Qian Wang,[a] Bingyu Zhao,[a] Xiaoyang Peng[a] and Ruiping Zhang *[b]

Received 10th November 2020
Accepted 5th January 2021

DOI: 10.1039/d0ra09545a

rsc.li/rsc-advances

Photoacoustic (PA) imaging has emerged as a promising bio-imaging technique due to its non-invasive visualization of lesions at great penetration depths. Fluorescence (FL) imaging in the second near-infrared window (NIR-II, 1000–1700 nm) achieves a higher imaging resolution and lower background signals compared to NIR-I. However, the single imaging method possesses its own disadvantages. Thus, we have demonstrated ZIF-8–IR820–MnPc–HA nanoparticles (ZIMH NPs) that can achieve visualization and localization of tumors in mice models with the help of a dual-modality PA/NIR-II FL imaging performance. Meanwhile, these excellent nanoparticles also induce the efficient generation of singlet oxygen ($^1O_2$) upon 808 nm laser illumination, and display excellent photodynamic therapy efficacy in cells, further indicating their potential application for *in vivo* PDT. In ZIMH NPs, hyaluronic acid (HA) impressively acts as a "sponge", enhancing the generation of $^1O_2$ and facilitating the cellular therapeutic effects. We believe that ZIF-8–IR820–MnPc–HA NPs present a brand-new strategy for the exploration of efficient PDT photosensitizers with dual-modality imaging performance for use in various biomedical applications.

1. Introduction

Malignant tumors, one of the most important causes of death, are becoming a serious threat to human health worldwide.[1–3] Thus, early and precise diagnosis plays a significant role in successful cancer therapy.[4] Although traditional medical imaging technologies, including ultrasonic imaging (USI), magnetic resonance imaging (MRI) and computed tomography (CT), can achieve accurate diagnosis by targeting clear organic lesions, patients have often missed the optimal treatment time due to the diagnosis not being timely enough.[5] In recent years, many emerging imaging strategies have been rapidly developed that can be applied to improve the early diagnosis of malignant tumors.[6] Among these strategies, photoacoustic imaging and fluorescence imaging are very interesting technologies. As a non-invasive and promising biomedical imaging technology, PA imaging offers efficient information in terms of anatomical, functional and molecular images by employing contrast agents that accumulate within a tumor to generate PA signals. More importantly, combined with the advantages of optical biomedical imaging and US imaging, PAI shows excellent contrast properties and deep penetrability, which have been successfully applied for the early detection of cancer.[7–9] As is well-known, FL imaging can be used to track and visualize diverse fluorescent probes without being invasive.[10] Previous FL imaging in the first near infrared window (NIR-I, 650–900 nm) cannot meet the demands of *in vivo* imaging with low penetration and high background signals. Compared to NIR-I FL imaging, FL imaging in the second near infrared window (NIR-II, 1000–1700 nm) has advantages of a higher imaging resolution and deeper tissue penetration.[11,12] Moreover, the signal-to-noise ratio of NIR-II FL imaging is greatly improved because of the weak tissue autofluorescence in the NIR-II window.[13] However, an individual imaging method alone is insufficient for providing more detailed information and has its own disadvantages.[14] Therefore, based on functional information provided by PAI and the distribution data of fluorescent probes revealed by FLI, the development of dual-modality imaging combining PA and FL imaging has become more urgent.[15] Many research efforts have been devoted to developing a dual-modality imaging probe. New indocyanine green (IR820), which has improved *in vitro* and *in vivo* stability compared to indocyanine green (ICG), is an NIR organic dye with suitable fluorescence and strong absorption in the NIR region.[16] More importantly, organic materials show a number of advantages over inorganic materials, such as

[a]*Department of Medical Imaging, First Clinical Medical College of Shanxi Medical University, Taiyuan 030001, P. R. China*

[b]*Department of Radiology, Third Hospital of Shanxi Medical University, Shanxi Bethune Hospital, Shanxi Academy of Medical Sciences, Department of Affiliated Bethune Hospital of Shanxi Medical University, Taiyuan 030001, P. R. China. E-mail: zrp_7142@163.com*

† Electronic supplementary information (ESI) available. See DOI: 10.1039/d0ra09545a

‡ The first two authors contributed equally to this work.

outstanding biocompatibility and potential biodegradability.[17] However, their practical clinical applications have still been hindered by a short half-life in blood, low cytotoxicity and their rapid clearance from the body.

A proper dual-modality imaging system alone can achieve early and accurate diagnosis of tumors, nevertheless, highly effective treatments are still important to thoroughly eradicate tumors. In recent years, photodynamic therapy (PDT) has emerged as a powerful tool to fight cancer, with well-defined advantages of high spatiotemporal selectivity, low invasiveness and negligible drug resistance.[18–20] Briefly, the photosensitizer (PS) is activated under laser irradiation, and this leads to the transition from light energy to molecular oxygen, which is then followed by the generation of reactive oxygen species (ROS) that induce effective cellular damage.[21–23] Furthermore, singlet oxygen ($^1O_2$) is also the most common species in PDT.[24] However, there is still an inevitable barrier that restricts the PDT effect due to the low penetration depth of light.[25] In order to overcome this problem, the activation of photosensitizers upon 808 nm laser illumination instead of the traditional 660 nm laser could be an effective method. For example, Younis *et al.* reported on a dual plasmonic photothermal therapy bonded indocyanine green, which could simultaneously achieve a PDT effect under single laser activation (808 nm) with a low power density and display excellent photothermal conversion efficiency.[26] Meanwhile, Zhang *et al.* designed an oxygen independent biomimetic nanoplatform based on carbon spheres dotted with cerium oxide and coated with a cell membrane, achieving a synergistic therapeutic effect against tumor cells depending on a photothermal effect and the generation of toxic hydroxyl radicals (·OH) under 808 nm laser irradiation.[27] Although a breakthrough in PDT upon 808 nm laser irradiation was achieved, systematic research has not yet been carried out. Thus, it is extremely urgent to develop highly effective photosensitizers for application in PDT, ensuring a deep penetration depth under irradiation by light of an appropriate wavelength. Typically, metal phthalocyanines (MPcs) possess an 18 π-electron conjugated planar architecture and, with weak absorption in the range of 400–600 nm, are associated with reduced skin phototoxicity and good (photo)chemical stabilities, making them excellent second-generation PS compounds.[25,28–30] Thus, MPcs could display excellent photodynamic properties but, unfortunately, poor solubility limits their optimal PDT efficacy. One important method for optimizing the PDT effect is to establish efficient nanocarriers for loading photosensitizers. However, ROS generation is still inhibited when much more PS is disorderly distributed, encapsulated in nanoparticles, and this may result in severe self-aggregation and singlet oxygen quenching.[31]

Mesoporous materials, such as metal–organic frameworks (MOFs), have widely been used for application in nanotechnologies, owing to their distinct structural features.[32] As is well-known, zeolitic imidazolate framework-8 (ZIF-8), composed of a zinc ion and 2-methylimidazolate, is an important species of porous material with desirable properties, including low toxicity, good biocompatibility, exceptional chemical stability, a well-defined porous structure and simple synthesis method.[33–36] Therefore, ZIF-8 is highly suitable as a nanocarrier to encapsulate functional molecules.

Taking the above reasons into consideration, in this work we have demonstrated multifunctional ZIF-8–IR820–MnPc–HA NPs that were designed to be applied in PA/NIR-II FL imaging (Scheme 1). As a naturally occurring polysaccharide, hyaluronic acid (HA) occurs in the extracellular matrix with high biocompatibility and biosafety.[37,38] In addition, HA with a low molecular weight also displays excellent water solubility. Due to these advantages, HA was coated around the surface of the ZIF-8–IR820–MnPc NPs. Interestingly, upon 808 nm laser irradiation, HA acted as a "sponge" in this nanosystem, and could help augment the generation of singlet oxygen species (Fig. 5B). More importantly, IR820 could be dispersed uniformly in the resulting porous structures of ZIF-8, and this was beneficial in reducing the quenching caused by the aggregation and enhancing the retention effect at the tumor site for *in vivo* NIR-II FL imaging. Therefore, ZIMH NPs can create a practical method for accurate tumor diagnosis guided by dual-modality PA/NIR-II FL imaging and can provide a promising PDT strategy for tumors in the future.

2. Experimental section

2.1. Materials

All agents were obtained from commercial suppliers without further purification. IR820 was purchased from Shanghai Yuanye Bio-Technology Co., Ltd. Manganese(II) phthalocyanine (MnPc) was obtained from Tianjin Alfa Aesar Chemical Co., Ltd. Zinc nitrate hexahydrate was acquired from Energy Chemical Co., Ltd. The Shanghai Aladdin Bio-Chem Technology Co., Ltd. supplied 2-methylimidazole. Hyaluronic acid (HA) was acquired from Dalian Meilun Biotech Co., Ltd. Methyl alcohol (MeOH) was purchased from Nanjing Kaitong Grain Biochemical R&D Co., Ltd. Cell Counting Kit-8 was purchased from Shanghai Yeasen Biotechnology Co., Ltd. 1,3-Diphenylisobenzofuran (DPBF) was purchased from Tokyo Chemical Industry Co., Ltd. Singlet Oxygen Sensor Green reagent (SOSG) and 2′,7′-dichlorofluorescein diacetate were obtained from Sigma-Aldrich. Absolute ethanol was acquired from Boster Biological Technology Co., Ltd.

2.2. Synthesis of the ZIMH NPs

The ZIMH NPs were prepared *via* a one-pot approach. First, MnPc (1 mg) was dissolved in MeOH (4 mL) under sonication and, subsequently $Zn(NO_3)_2 \cdot 6H_2O$ (60 mg) was added into the above solution under stirring in the dark for 10 min. After that, a 2 mL of MeOH solution of IR820 (12 mg) was added dropwise into the above mixture, accompanied with stirring for 10 min. Then, a 4 mL of a MeOH solution of 2-methylimidazole (132 mg) was added to continue the reaction. After stirring for 30 min, the reaction mixture was centrifuged and washed with MeOH three times. The mixture was added into deionized water (20 mL) containing HA (2 mg) under stirring overnight. The complexes were centrifuged and washed several times and, finally, the powdered ZIMH NPs were obtained by freeze-drying.

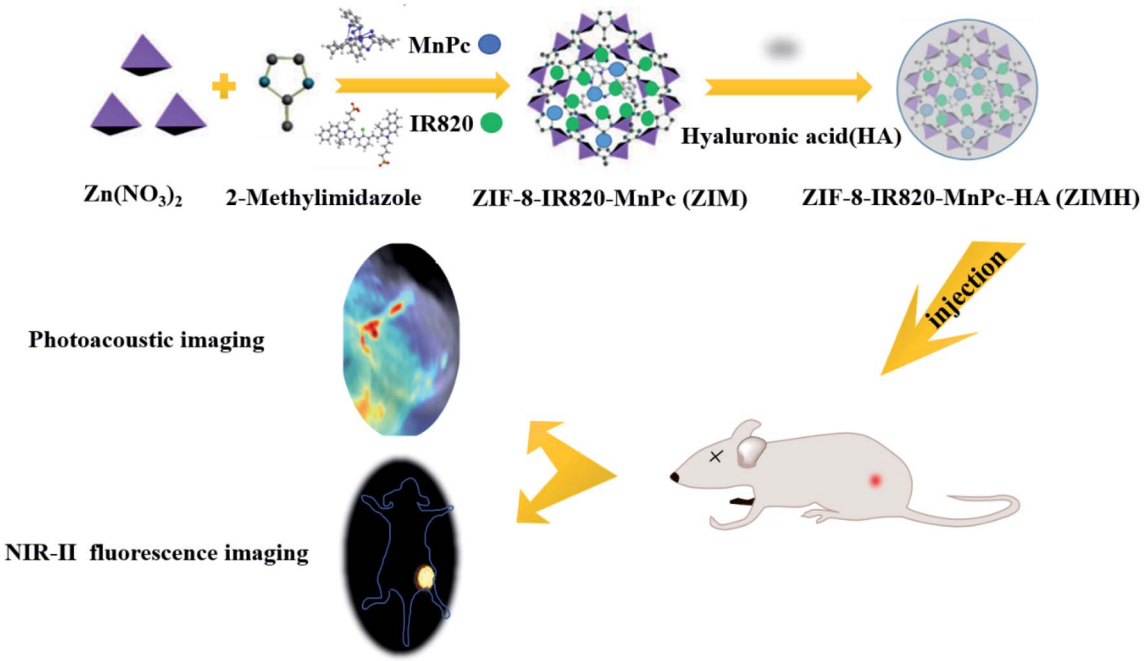

Scheme 1 Schematic diagram of the synthesis of ZIF-8–IR820–MnPc–HA nanoparticles and of the *in vivo* dual-modality imaging process.

2.3. Characterization

We used a JEM-2100F microscope (JEOL, Japan) to record transmission electron microscopy (TEM) images of ZIM and the ZIMH NPs. The dynamic light scattering (DLS) experiments of ZIMH were carried out with a Nano-Zetasizer (Malvern Instruments Ltd.). A UV-Vis-NIR spectrometer (UV-6100, MAPADA) was used to obtain the absorption spectra of ZIF-8, MnPc, IR820 and ZIM. Thermogravimetric analysis (Setsys Evolution TGA 16/18) was performed at a heating rate of 5 °C min^{-1} under a N_2 atmosphere. Infrared spectroscopy was recorded on a TENSOR II Fourier-transform infrared (FTIR) spectrometer (Bruker, Germany).

2.4. Singlet oxygen generation detection in aqueous solution

The generation of singlet oxygen ($^1O_2$) was investigated by chemical probes. First, DPBF was utilized to determine the production of singlet oxygen. In brief, 60 μL of DPBF (1 mg mL^{-1}) and different samples including ZIF-8–MnPc, ZIF-8–IR820, ZIF-8–MnPc–IR820 and ZIF-8–IR820–MnPc–HA (200 μg mL^{-1}) were mixed under stirring in the dark. Then, the resulting mixtures were irradiated with a 808 nm laser (1.0 W cm^{-2}) for 30 s, followed by detection using a UV-Vis spectrophotometer at 416 nm wavelength every 4 min. Then, SOSG was introduced to further detect $^1O_2$. 1 mL of SOSG (5 μmol L^{-1}) and 2 mL of the four samples (50 μg mL^{-1}) were mixed well in tubes for 5 min. Then, the tubes containing the different materials experienced illumination with a 808 nm laser (0.5 W cm^{-2}) for 1 min. Finally, the SOSG fluorescence intensity was measured with an excitation of 504 nm and an emission of 525 nm using a NIR-II spectrophotometer (Series III 900/1700).

2.5. Cell culture and animal tumor model

Cell culture. The 4T1 (mouse breast cancer) cell line was purchased from the China Center for Type Culture Collection (Wuhan, China) and was cultured in RPMI 1640 medium containing 10% fetal bovine serum (FBS) at 37 °C under a 5% CO_2 containing atmosphere.

Animal tumor model. The animal procedures were performed in accordance with the Guidelines for Care and Use of Laboratory Animals of Shanxi Medical University, and the experiments were approved by the Animal Ethics Committee of Shanxi Medical University. The Beijing Vital River Experimental Animal Company supplied the six-week-old female BALB/c nude mice (16–18 g). After 2 weeks of acclimatization, 4T1 tumors were established by the subcutaneous injection of 4T1 cells suspended in 50 μL of PBS (3×10^6) into the right thigh area of each mice. Then, the mice were observed daily for any behavioral abnormalities and the tumor size was monitored and recorded periodically. The tumor-bearing mice were used for *in vivo* imaging experiments when the tumor volumes approached 80–100 mm^3.

2.6. Cellular experiments

Cell viability assay. The cytotoxicity of the ZIMH NPs was estimated by a Cell Counting Kit-8 (CCK-8) assay. Briefly, 4T1 cells were seeded in 96-well plates at a density of 8000 cells per well and were left to establish overnight. Afterwards, the old medium was replaced with fresh RPMI 1640 medium containing ZIMH at various concentrations (0, 3.125, 6.25, 12.5, 25 and 50 μg mL^{-1}), followed by incubation for 12 h at 37 °C under a 5% CO_2 containing atmosphere. Then, the dead cells were washed with PBS three times and the remaining live cells were

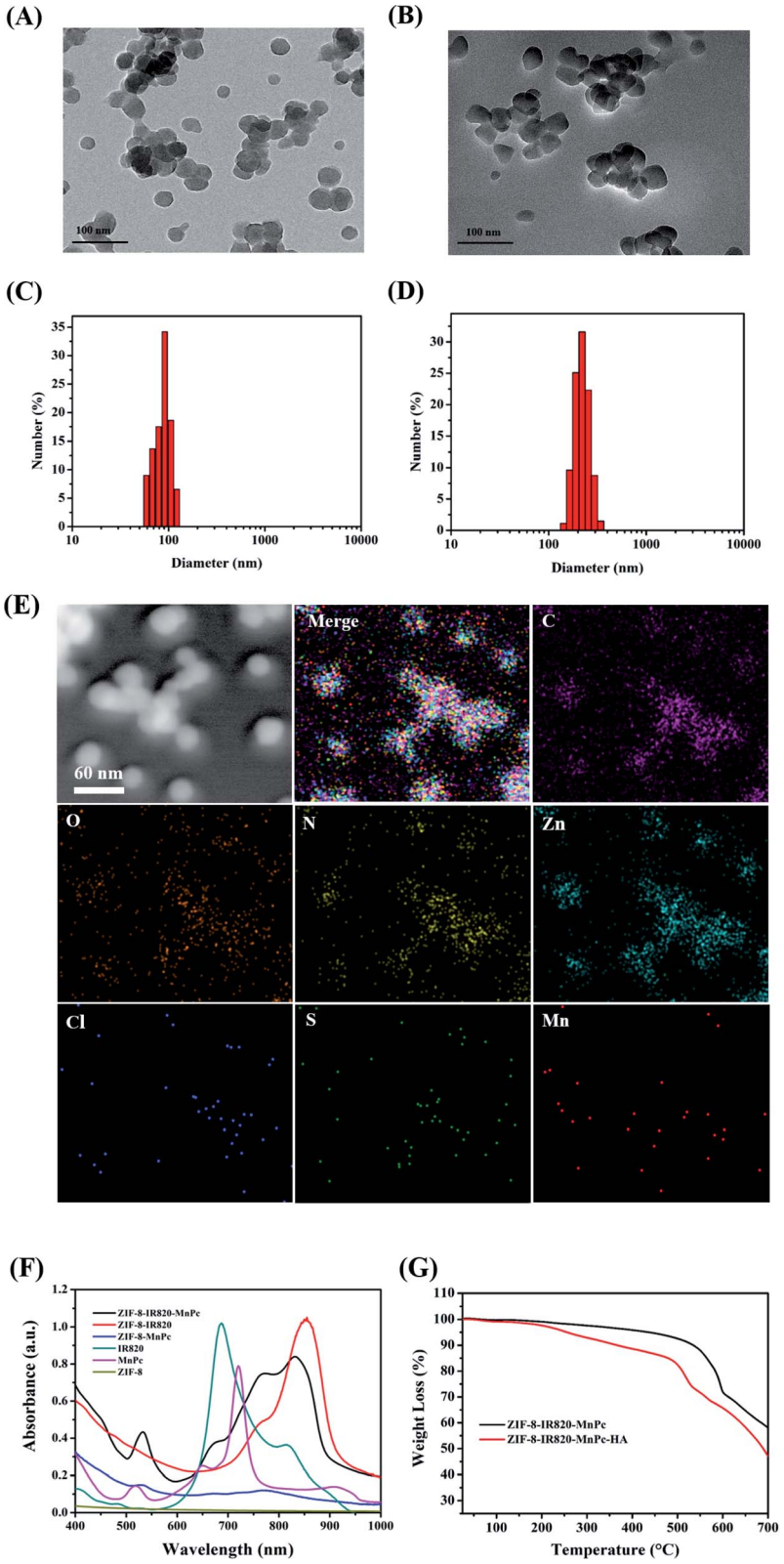

Fig. 1 TEM images and DLS data (A–D) of the ZIF-8–IR820–MnPc nanoparticles and ZIF-8–IR820–MnPc–HA nanoparticles. (E) TEM-EDS mapping of ZIMH NPs. (F) The UV-Vis absorption spectra of ZIF-8, IR820, MnPc, ZIF-8–IR820, ZIF-8–MnPc and ZIF-8–IR820–MnPc nanoparticles. (G) Thermogravimetric analysis of ZIM and ZIMH NPs.

incubated in new medium containing 10% CCK-8 for 1 h in the dark. Finally, the absorbance of each well was measured at 450 nm and was recorded using a microplate reader (SpectraMax Plus 384).

Singlet oxygen generation detection in cells. In order to monitor the intracellular singlet oxygen generation, 4T1 cells were seeded at a density of 2×10^4 cells per well on four-well plates for 12 h. Then, the cells were incubated with ZIMH NPs (10 μg mL^{-1}) for 3 h. After each well was washed with PBS three times, serum-free 1640 RPMI medium containing DCFH-DA (20 μM) was added for a further 30 min incubation period, and this was then followed by illumination with a 808 nm laser under a density power of 0.5 W cm^{-2} for 5 min. Finally, fluorescence images of the production of singlet oxygen were obtained using an inverted fluorescence microscope (Olympus IX73).

Photodynamic therapy in cells. 4T1 cells were also used to evaluate the efficacy of the photodynamic therapy of ZIF-8–IR820–MnPc–HA. Cells were seeded into a 96-well plate at a density of 8000 cells per well overnight. Then ZIF-8–IR820–MnPc–HA (50 μg mL^{-1}) was added into each well for a sufficient incubation period. After exposure to NIR laser (808 nm, 0.2 W cm^{-2}) radiation for 5 min, the cells were stained with calcein AM and PI for 20 min to verify the photodynamic therapy on cancer cells and to distinguish the live cells (green color) and dead cells (red color), and these were finally imaged using a fluorescence microscope.

2.7. PA imaging *in vitro*

The PA effect of ZIMH was evaluated by a multispectral optoacoustic tomographic (MSOT) imaging system (inVision 128, iThera Medical GmbH, Neuherberg, Germany) from 680 to 980 nm. Then, various concentrations of ZIMH (25, 50, 100, 200 and 400 μg mL^{-1}) were injected into phantoms, which were measured using a PA detector at 880 nm. Finally, the correlation curve between PA intensity and concentration was plotted.

2.8. NIR-II FL imaging *in vitro*

In order to estimate the NIR-II FL effect of ZIMH *in vitro*, different concentrations of ZIMH solution at 0.0625, 0.125, 0.25, 0.5 and 1 mg mL^{-1} were added into 200 μL tubes, respectively, and the images were recorded using a fluorescence imaging instrument (Series III 900/1700).

2.9. PA/NIR-II fluorescence dual-modality *in vivo* imaging

When the tumors reached a volume of 80–100 mm^3, the 4T1 tumor-bearing nude mice were intratumorally injected with ZIMH (200 μL, 5 mg mL^{-1}). The PA and FL images were acquired at different time points (0, 0.1, 1, 2, 4, 6 and 12 h). Then, analysis of the imaged data was carried out by the ImageJ and MSOT imaging system software, respectively. Quantitative analysis was obtained through the ImageJ software.

3. Results and discussion

3.1. Characterization

The final product ZIMH NPs displayed good biocompatibility due to the introduction of hyaluronic acid (HA). TEM images revealed that the size of the obtained ZIF-8–IR820–MnPc NPs increased from 30.0 to 45.0 nm after the surface was coated with HA and this was accompanied by an irregular shape (Fig. 1A and B). The corresponding dynamic light scattering (DLS) data in the inset of the ZIM and ZIMH NPs is shown in Fig. 1C and D. Compared with the ZIF-8–IR820–MnPc NPs (approximately 145.0 nm), the ZIF-8–IR820–MnPc–HA NPs exhibit high dispersity in deionized water with larger narrow hydrated size distribution centered at 213.9 nm. According to the transition of nanoparticle size, we could deduce the successful synthesis of ZIM and the introduction of HA into ZIM NPs. The FTIR spectra shown in Fig. S1† display the existence of the structure of ZIF-8 in ZIF-8–IR820–MnPc NPs. Due to low dye loading, the IR spectra of the different samples only show the infrared absorption spectra of ZIF-8. Based on the different colors of the raw materials and products (Fig. S2†), we can trust in the correct synthesis of ZIM NPs. In order to reveal the components of the nanoparticles, the elemental TEM mapping images of ZIMH NPs were obtained and are depicted in Fig. 1E. It is clear that the C, N, O, Zn, Cl, S and Mn elements are well-distributed in the structures, and this provides further evidence for particle structure and distribution of elements in the ZIMH NPs. The energy-dispersive X-ray spectrum (EDS), shown in Fig. S3,† is in agreement with the results shown in Fig. 1E, as described. In addition, the UV-Vis spectra (Fig. 1F) showed that the maximum absorption peak of IR820 was located at 820 nm, while MnPc exhibited a peak absorption wavelength at 520 nm. The ZIM NPs have overlapping absorption with the two dyes, confirming the successful synthesis of the ZIM NPs. Thus, a dual-modality nanoplatform motivated by a single NIR laser (808 nm) could be constructed, where IR820 could be applied to photoacoustic imaging and NIR-II fluorescence imaging, respectively. Thermogravimetric analysis (TGA) is a useful method to examine the amount of HA in the ZIMH NPs. As shown in Fig. 1G, the successful coating of ZIM NPs can be verified and the mass fraction of HA in the ZIMH NPs is 10%.

3.2. Singlet oxygen generation ability in solution

To verify the photodynamic performance of the ZIMH solution, 1,3-diphenylisobenzofuran (DPBF), a molecular probe commonly used to detect singlet oxygen, was used to monitor reactive oxide species (ROS) production under NIR light irradiation (Fig. 2A–E). The characteristic absorption peak of DPBF at 416 nm significantly decreased, preliminarily confirming $^1O_2$ generation. In Fig. 2A–C, the ZIF-8–MnPc, ZIF-8–IR820 and ZIF-8–IR820–MnPc NPs under 808 nm laser irradiation displayed a slight time-dependent decrease in DPBF absorption, indicating that these materials generate negligible $^1O_2$. In contrast, the ZIMH NPs under 808 nm laser irradiation (0.5 W cm^{-2}) demonstrated a clear decrease in the DPBF absorption peak at 416 nm, suggesting efficient $^1O_2$ generation

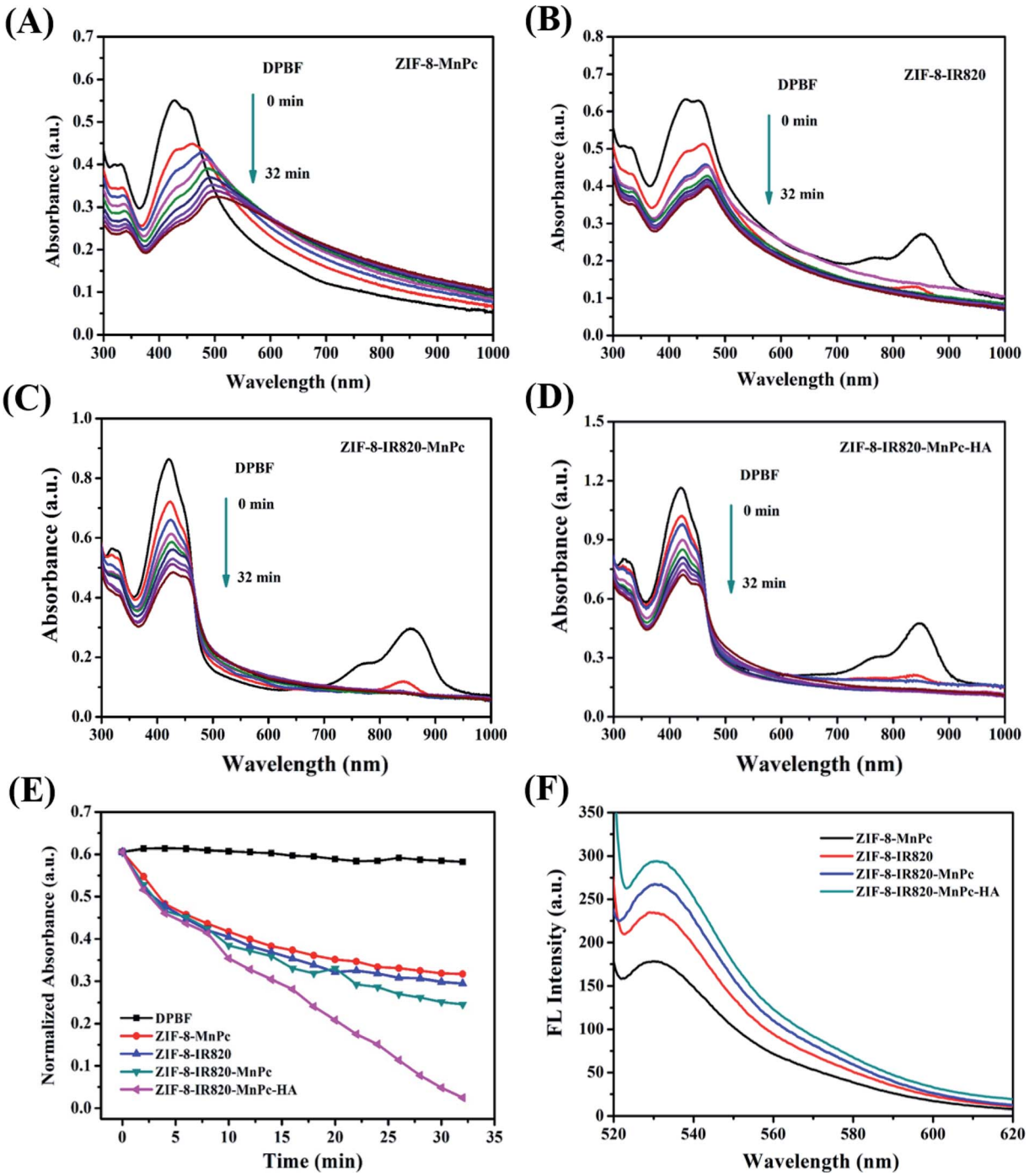

Fig. 2 Time-dependent decrease in the UV-Vis absorption spectra of DPBF treated with (A) ZIF-8–MnPc (200 μg mL^{-1}), (B) ZIF-8–IR820 (200 μg mL^{-1}), (C) ZIF-8–IR820–MnPc (200 μg mL^{-1}) and (D) ZIF-8–IR820–MnPc–HA (200 μg mL^{-1}) NPs. (E) Normalized absorbance profiles of DPBF as a control, ZIF-8–MnPc, ZIF-8–IR820, ZIF-8–IR820–MnPc and ZIF-8–IR820–MnPc–HA under 808 nm laser irradiation (1.0 W cm^{-2}). (F) Time-dependent increase in the SOSG fluorescence intensity treated with the solutions mentioned above (50 μg mL^{-1}) and 808 nm laser irradiation (0.5 W cm^{-2}).

with the help of MnPc and IR820 (Fig. 2D). As depicted in Fig. 2E, there was no significant change in the time-dependent absorbance of DPBF alone. Furthermore, among these materials, only the ZIMH NPs exhibited a higher DPBF oxidation rate under laser irradiation, implying the effective generation of ROS in the ZIMH NPs.

Next, another highly-sensitive $^1O_2$ indicator singlet oxygen sensor green (SOSG) was introduced to investigate the $^1O_2$ generation ability of ZIMH NPs, as shown in Fig. 2F. Similarly, the $^1O_2$ generation was determined by gradual increments in the SOSG emission peak at 530 nm. As shown in Fig. 2F, upon irradiation, the ZIMH NPs showed considerably high SOSG

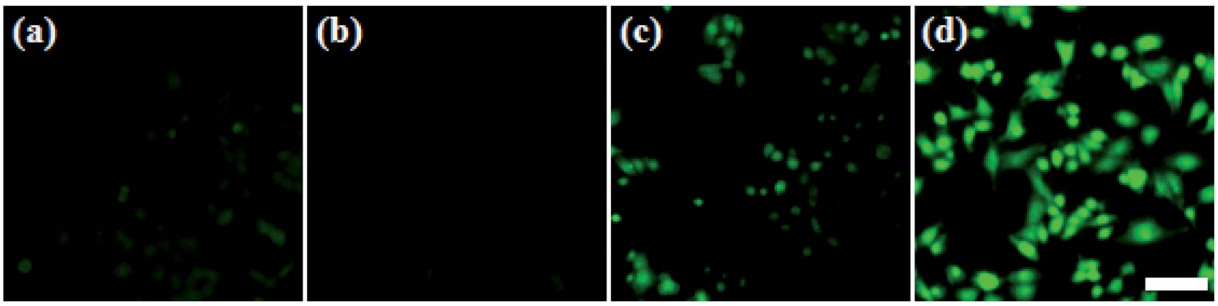

Fig. 3 Fluorescence images of 4T1 cells incubated with DCFH-DA (20 μM) with different treatments: (a) control; (b) 808 nm laser irradiation for 5 min; (c) ZIMH NPs; (d) ZIMH NPs plus 808 nm laser irradiation for 5 min. Scale bar: 20 μm.

fluorescence intensity, and this was consistent with the results tested by DPBF, suggesting an $^1O_2$ generation ability of ZIMH NPs. In the cases of ZIF-8–MnPc, ZIF-8–IR820 and ZIF-8–IR820–MnPc, we could preliminarily consider that there was insignificant $^1O_2$ generation due to only slight augmentation in the SOSG fluorescence intensities.

3.3. Singlet oxygen generation detection in cells

In addition, in order to evaluate the cellular $^1O_2$ generation ability of the ZIMH NPs with different treatments, 2,7-dichlorofluorescein diacetate (DCFH-DA) was used as the ROS indicator that will emit green fluorescence in the presence of endogenous ROS (Fig. 3). Live 4T1 cells were pretreated with the ZIMH NPs and incubated with DCFH-DA. Fig. 3a shows the fluorescence images with 4T1 cells as a control. It can also be seen that the 4T1 cells treated with ZIMH NPs (Fig. 3b) or laser irradiation (Fig. 3c) only displayed faint green fluorescence. The bright green signal from the ROS can only be observed in Fig. 3d, when the cells were treated with ZIMH NPs under 808 nm laser irradiation at a power density of 0.5 W cm^{-2}, confirming the intracellular generation of $^1O_2$.

3.4. *In vitro* cytotoxicity assay

As is well-known, the negligible toxicity and excellent biocompatibility of nanoparticles are prerequisites for *in vivo* application.[39] Therefore, the cytotoxicity of the multifunctional composite was evaluated using standard CCK-8 assays on 4T1 cells. As depicted in Fig. 4A, most of the 4T1 cells remained alive after being incubated with ZIMH NPs for 12 h at different concentrations. Even at a high concentration of up to 50 μg mL^{-1}, more than 90% of the 4T1 cells were still alive, suggesting negligible cytotoxicity of ZIMH NPs. Therefore, we selected this optimal nanoparticle dose of 50 μg mL^{-1} for all following *in vivo* experiments in this study. Subsequently, Fig. 4B briefly illustrates the schematic diagram of the ROS behavior potentiated by hyaluronic acid in a tumor microenvironment. Upon 808 nm laser irradiation, $^1O_2$ was uniformly distributed onto the surface of the hyaluronic acid of the ZIMH NPs, rather than being released rapidly into the tumor microenvironment, and this can be explained by the sponge effect induced by HA. Furthermore, the calcein AM and PI results, shown in Fig. S4,† demonstrated the primary PDT performance of the ZIF-8–IR820–MnPc–HA nanoparticles. In Fig. S4a–c,† many cells were still alive (green color) and there was no obvious cell death in either the control or single variable (laser alone or ZIMH alone) groups. Only

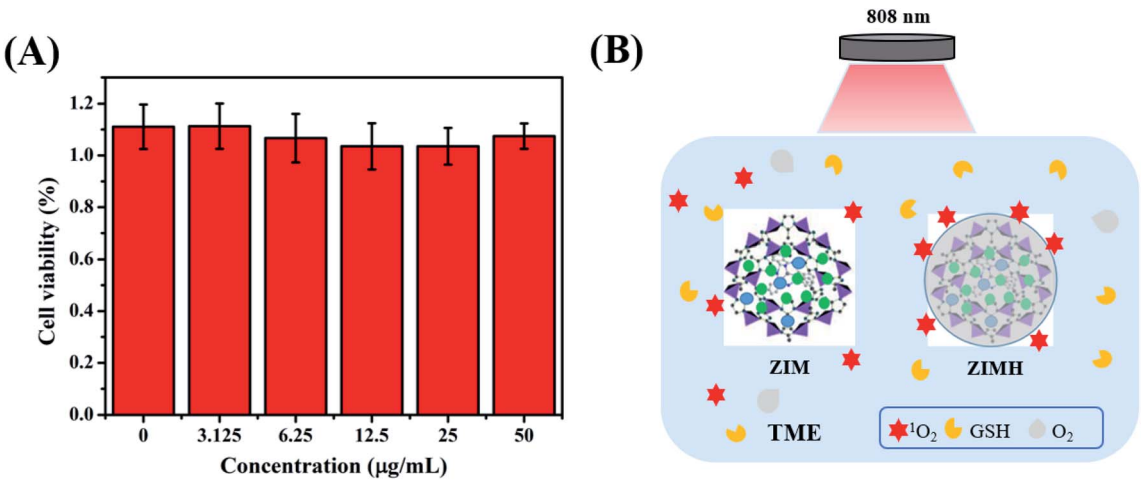

Fig. 4 (A) Relative viabilities of 4T1 cells incubated with ZIMH NPs at various concentrations by CCK-8 assay. (B) Schematic illustration of the ROS behaviors potentiated by hyaluronic acid.

when the cells were treated with ZIMH (50 μg mL^{-1}) with a 808 nm laser at a density of 0.5 W cm^{-2}, was there any obvious cell death (red color) (Fig. S4d†).

3.5. PA imaging *in vitro* and *in vivo*

To better achieve *in vivo* PA imaging, we first evaluated the PA imaging ability *in vitro*. As shown in Fig. 5A, we found through *in vitro* phantom tests that the photoacoustic intensities of the ZIMH NPs had good linear correlations with their concentrations within a range from 25 to 400 μg mL^{-1}, indicating the good feasibility of PA imaging for *in vivo* experiments. Additionally, responsive PA images of various solutions were obtained using a multispectral optoacoustic tomographic (MSOT) imaging system.

Accurately locating tumor areas is significantly vital for further therapy. Due to the high sensitivity of optical imaging, outstanding resolution and a favorable tissue penetration depth of several centimeters,[40] PAI is a promising imaging modality that could achieve real-time tracking of the distribution of nanoparticles *in vivo*. Thus, 4T1 tumor-bearing nude mice were subsequently examined with the MSOT system. Then, PA intensity changes in the tumor site were demonstrated before and after the tumor-bearing mice were treated with intratumor injections of ZIMH NPs (5 mg mL^{-1}) at 0 h, 0.1 h, 1 h, 2 h, 4 h, 6 h and 12 h (Fig. 5B), and the photoacoustic images were recorded in a time-dependent manner (Fig. 5C). It is worth noting that the PA signals of the ZIMH NPs in the tumor sites gradually increased after injection, reaching a maximum level at 1 h post-injection. Then, the retained photoacoustic signals of ZIMH began to decline over time. After 12 h post-injection, the PA signal nearly disappeared. Therefore, we are able to take a preliminary view that ZIMH can be expected to be applied in photoacoustic imaging in the clinic.

3.6. NIR-II FL imaging *in vitro* and *in vivo*

Fig. 6A presents the emission spectrum of the ZIMH NPs. It is worth noting that the emission spectrum of ZIMH in water could even extend to longer than 1100 nm. Considering the emission spectrum of ZIMH, the NIR-II fluorescence imaging results were also analyzed using a fluorescence imaging instrument. Furthermore, the fluorescence images were inserted into the emission spectrum.

In the subsequent FL imaging experiments, all mice were treated with an intratumor injection of ZIMH NPs (200 μL, 5 mg mL^{-1}). Inspired by the FL imaging results *in vitro*, we then demonstrated the NIR-II FL imaging performances for the visualization of tumor size, shape, and location. The autofluorescence signals of the mice were deducted by spectral unmixing in the Cy-5.5 channel. The FL intensity changes in the tumor site were acquired using ImageJ software, and were roughly consistent with those of PA at the corresponding sites (Fig. 6B). Then, FL images of the tumor-bearing mice were

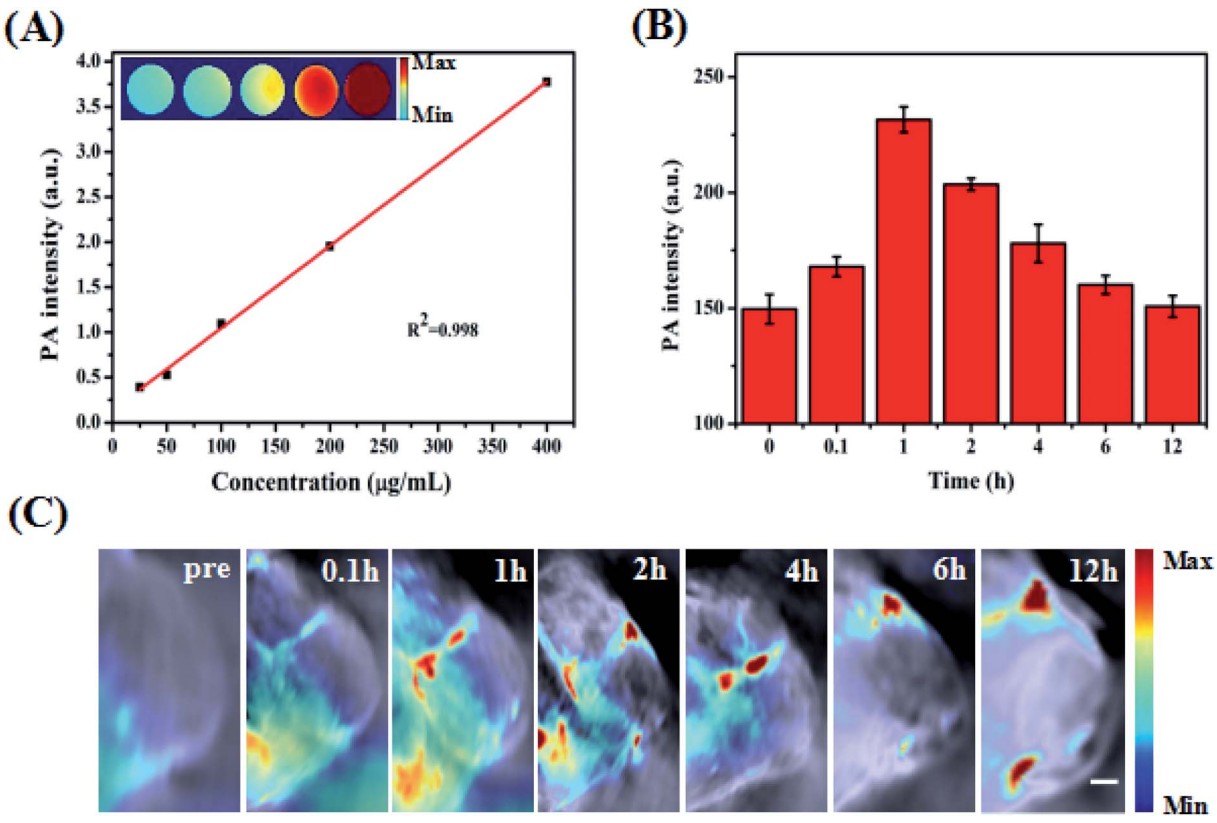

Fig. 5 Photoacoustic imaging *in vitro* and *in vivo*. (A) The linear relationship between the PA intensity and concentrations of ZIMH with corresponding PA images is shown in the inset. (B) *In vivo* PA intensity changes of the tumor site of tumor-bearing mice before and after intratumor injection at 0.1 h, 1 h, 2 h, 4 h, 6 h and 12 h. (C) PA images of the tumors at different time points. Scale bars: 1.0 mm.

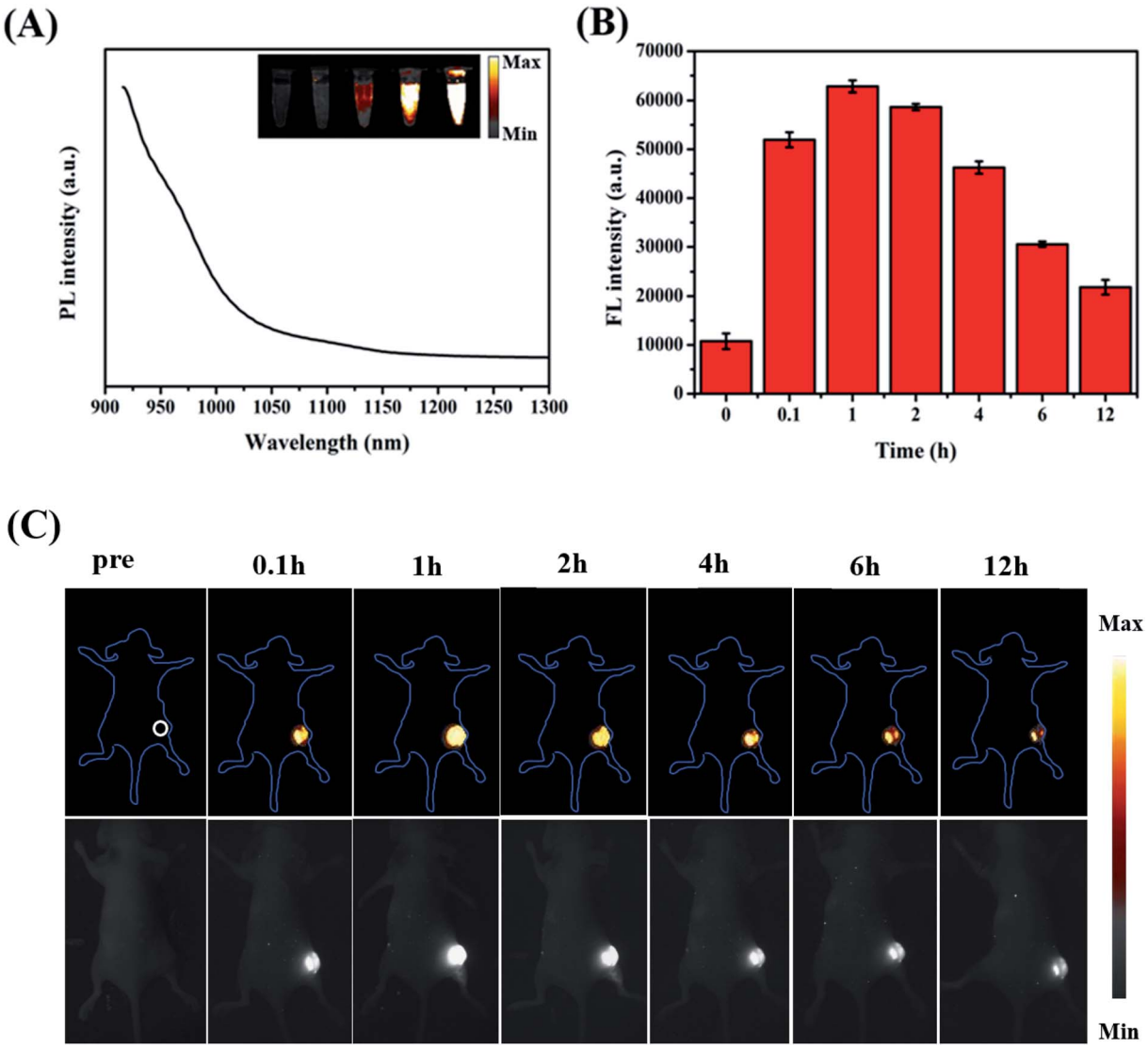

Fig. 6 NIR-II fluorescence imaging *in vitro* and *in vivo*. (A) NIR-II fluorescence emission spectrum of ZIMH with corresponding FL images in the inset. (B) *In vivo* NIR-II FL intensity changes of the tumor site of tumor-bearing mice before and after intratumor injection at 0.1 h, 1 h, 2 h, 4 h, 6 h and 12 h. (C) NIR-II FL images of the tumor-bearing mice at different time points.

recorded and are shown in Fig. 6C. After injection with ZIMH NPs, FL signals gradually filled the tumor site. It was clearly found that the NIR-II fluorescence signals of the ZIMH NPs also reached a peak after 1 h post-injection and could be observed almost throughout the whole tumor. Afterwards, the FL signal of the tumor site became weak and gradually disappeared after 12 h post-injection. Taken together, these results indicate that ZIMH has excellent FL imaging capability for early diagnosis in the NIR-II window.

3.7. *In vivo* biosafety

Blood biochemistry examination was used to evaluate potential toxic effects of the nanoparticles, which can be used to monitor the response to nanoparticle exposure and is widely used in disease diagnoses of the liver and kidney. Among them, ALT and AST are crucial enzymes in the liver and are commonly used as markers of liver disorders or injury, while BUN and SCr are good indicators of kidney damage. The corresponding blood biochemistry examination was performed after injection (200 μL, 5 mg mL^{-1}) at 1 d and 7 d. In Fig. 7A and B, no obvious increase in ALT or AST is observed in the ZIMH NPs group compared with the results of the control group, and the levels of BUN and SCr are not significantly different from those of the saline group. Then, the biotoxicity of the ZIMH NPs was also validated through histological analysis of significant organs (heart, liver, spleen, lung, and kidney) *via* H&E staining. The results in Fig. 7C indicate that minimal side effects of the nanoparticles could be observed in different organs of the mice treated with the ZIMH NPs. All these results indicate that the ZIF-8–IR820–MnPc–HA NPs has good biocompatibility and negligible toxicity.

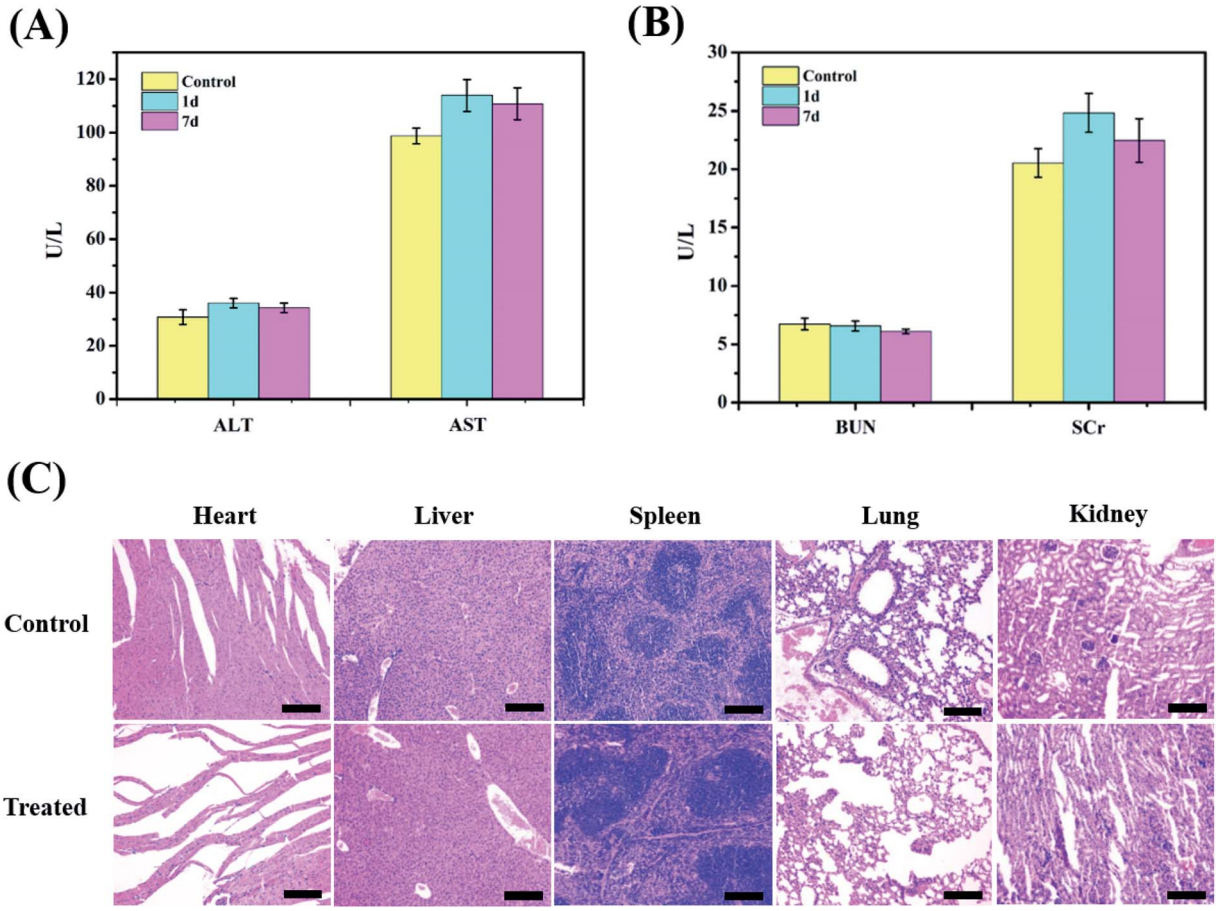

Fig. 7 *In vivo* toxicity. (A and B) Blood chemistry indexes (ALT, AST, BUN and SCr) of the mice in the control group and in the treated groups with ZIF-8–IR820–MnPc–HA NPs after 1 day and after 7 days. (C) Images of H&E-stained major organs (heart, liver, spleen, lung and kidney) from healthy control mice and the ZIMH-injected mice after 24 h. Scale bar: 200 μm.

4. Conclusion

In summary, we have demonstrated ZIMH NPs that can generate singlet oxygen upon 808 nm laser irradiation, showing improved PDT property. The nanoparticles also exhibited excellent *in vivo* dual-modality PA/NIR-II FL imaging. More importantly, the HA coated on the surface of the ZIMH NPs could act as a sponge, enhancing the generation of $^1O_2$ and facilitating the cellular therapeutic effects. Through this protective sponge effect, created by HA, IR820 showed remarkable NIR-II FL imaging performance due to the long-circulation. Overall, this work has generated ZIMH NPs as a practical dual-modality PA/FL nanoplatform that can be used for early and precise diagnosis of tumors, and the PDT effect of the NPs is expected to be further developed in following work.

Conflicts of interest

The authors declare no conflicts of interest.

Acknowledgements

This work was financially supported by the National Natural Science Foundation of China (No. 81571747 and 81771907), the Science and Technology Innovation Team Project of Shanxi Province (No. 201705D131026), the Engineering Technology Research Center of Shanxi Province (No. 201805D121008), the Scientific and Technological Achievements Transformation Project of Shanxi Province (No. 201704D131006), the Laboratory Construction Project of Shanxi Province, the Projects for Local Science and Technology Development guided by the Central Committee (YDZX20191400002537), the Natural Science Foundation of Shanxi Province (No. 201901D111213), the Startup Foundation for Doctors of Shanxi Medical University (No. 03201505), and the Postgraduate Education Innovation Project of Shanxi Province (2020SY225).

References

1 K. D. Miller, L. Nogueira, A. B. Mariotto, J. H. Rowland, K. R. Yabroff, C. M. Alfano, A. Jemal, J. L. Kramer and R. L. Siegel, *Ca-Cancer J. Clin.*, 2019, **69**, 363–385.
2 X. Wang, X. Zhong, L. Bai, J. Xu, F. Gong, Z. Dong, Z. Yang, Z. Zeng, Z. Liu and L. Cheng, *J. Am. Chem. Soc.*, 2020, **142**, 6527–6537.
3 W. Zhang, S. Song, H. Wang, Q. Wang, D. Li, S. Zheng, Z. Xu, H. Zhang, J. Wang and J. Sun, *Biomaterials*, 2019, **217**, 119279.

4 Q. Li, S. Li, S. He, W. Chen and K. Pu, *Angew. Chem.*, 2020, **132**, 7084–7089.
5 Z. Yang, Y. Du, Q. Sun, Y. Peng, R. Wang, Y. Zhou, Y. Wang, C. Zhang and X. Qi, *ACS Nano*, 2020, **14**, 6191–6212.
6 R. Zhu, L. Su, J. Dai, Z. Li, S. Bai, Q. Li, X. Chen, J. Song and H. Yang, *ACS Nano*, 2020, **14**, 3991–4006.
7 Q. Fu, Z. Li, J. Ye, Z. Li and J. Song, *Theranostics*, 2020, **10**, 4997–5010.
8 Q. Fu, R. Zhu, J. Song, H. Yang and X. Chen, *Adv. Mater.*, 2019, **31**, 1805875.
9 Y. Liu, P.-C. Wu, S. Guo, P.-T. Chou and T.-M. Liu, *Photoacoustics*, 2020, **19**, 100179.
10 X. Ge, Y. Lou, L. Su, B. Chen and H. Yang, *Anal. Chem.*, 2020, **92**, 6111–6120.
11 X. Ge, Q. Fu, L. Su, Z. Li and J. Song, *Theranostics*, 2020, **10**, 4809–4821.
12 F. Zhang, B. Li, L. Lu, M. Zhao and Z. Lei, *Angew. Chem.*, 2018, **57**, 7483–7487.
13 Z. Feng, X. Yu, M. Jiang, L. Zhu and J. Qian, *Theranostics*, 2019, **9**, 5706–5719.
14 K. Wu, H. Zhao, Z. Sun, B. Wang and W. Huang, *Theranostics*, 2019, **9**, 7697–7713.
15 J. Qu, D. Teng, G. Sui, S. Guan, Y. Wang, Q. Wang, Y. Lin, H. Ran, Z. Wang and H. Wang, *Biomater. Sci.*, 2020, **8**, 3116–3129.
16 X. Hu, H. Tian, W. Jiang, A. Song, Z. Li and Y. Luan, *Small*, 2018, **14**, 1802994.
17 X. Lu, P. Yuan, W. Zhang, Q. Wu, X. Wang, M. Zhao, P. Sun, W. Huang and Q. Fan, *Polym. Chem.*, 2018, **9**, 3118–3126.
18 T. Luo, K. Ni, A. Culbert, G. Lan, Z. Li, X. Jiang, M. Kaufmann and W. Lin, *J. Am. Chem. Soc.*, 2020, **142**, 7334–7339.
19 W. Sun, L. Luo, Y. Feng, Y. Qiu, C. Shi, S. Meng, X. Chen and H. Chen, *Adv. Mater.*, 2020, **32**, e2000377.
20 Y. Cai, D. Ni, W. Chen, C. Ji, Y. Wang, M. Müllen, Z. Su, Y. Liu, C. Chen and M. Yin, *Angew. Chem., Int. Ed.*, 2020, **59**, 14014–14018.
21 J. Chen, K. Wen, H. Chen, S. Jiang, X. Wu, L. Lv, A. Peng, S. Zhang and H. Huang, *Small*, 2020, **16**, 2000909.
22 F. D. Duman, M. Sebek, N. T. K. Thanh, M. Loizidou and A. J. MacRobert, *J. Mater. Chem. B*, 2020, **8**, 5131–5142.
23 J. Wang, J. Sun, W. Hu, Y. Wang, T. Chou, B. Zhang, Q. Zhang, L. Ren and H. Wang, *Adv. Mater.*, 2020, **32**, 2001862.
24 H. Wang, Z. Wang, Y. Li, T. Xu, Q. Zhang, M. Yang, P. Wang and Y. Gu, *Small*, 2019, **15**, 1902185.
25 Z. Wang, T. Jia, Q. Sun, Y. Kuang, B. Liu, M. Xu, H. Zhu, F. He, S. Gai and P. Yang, *Biomaterials*, 2020, **228**, 119569.
26 M. Younis, C. Wang, R. An, S. Wang, M. Younis, Z. Li, Y. Wang, A. Ihsan, D. Ye and X. Xia, *ACS Nano*, 2019, **13**, 2544–2557.
27 C. Zhang, W. Liu, X. Bai, S. Cheng, Z. Zhong and X. Zhang, *Biomaterials*, 2019, **199**, 1–9.
28 J. Pan, A. Ouyang, W. Fang, G. Cheng, W. Liu, F. Wang, D. Zhao, K. Le and J. Jiang, *J. Mater. Chem. B*, 2020, **8**, 2895–2908.
29 M. Cacioppo, T. Scharl, L. Đordevic, A. Cadranel, F. Arcudi, D. Guldi and M. Prato, *Angew. Chem., Int. Ed.*, 2020, **59**, 12779–12784.
30 P. Lo, M. Rodriguez-Morgade, R. Pandey, D. K. P. Ng, T. Torres and F. Dumoulin, *Chem. Soc. Rev.*, 2020, **49**, 1041–1056.
31 X. Tong, S. Gan, J. Wu, Y. Hu and A. Yuan, *Nanoscale*, 2020, **12**, 7376–7382.
32 J. Zhao, X. Quan, S. Chen, Y. Liu and H. Yu, *ACS Appl. Mater. Interfaces*, 2017, **9**, 28685–28694.
33 A. Maleki, M. Shahbazi, V. Alinezhad and H. Santos, *Adv. Healthcare Mater.*, 2020, e2000248, DOI: 10.1002/adhm.202000248.
34 J. Feng, W. Yu, Z. Xu, J. Hu, J. Liu and F. Wang, *ACS Appl. Mater. Interfaces*, 2020, **12**, 22613–22623.
35 M. Wang, Z. Mao, L. Liu, L. Peng, N. Yang, J. Deng, W. Ding, J. Li and Z. Wei, *Small*, 2018, **14**, e1804183.
36 Y. Kang, X. Yu, X. Fan, D. Ao, S. Zhao, C. Tu, Z. Yan, R. Wang, W. Li and H. Qiu, *ACS Nano*, 2020, **14**, 4336–4351.
37 H. Duan, M. Donovan, F. Hernandez, C. Primo, E. Garanger, X. Schultze and S. Lecommandoux, *Angew. Chem., Int. Ed.*, 2020, **59**, 13591–13596.
38 Q. Xu, X. Li, P. Zhang and Y. Wang, *J. Mater. Chem. B*, 2020, **8**, 4331–4339.
39 J. Yang, F. Gao, D. Han, L. Yang, X. Kong, M. Wei, J. Cao, H. Liu, Z. Wu and G. Pan, *Mater. Des.*, 2018, **139**, 172–180.
40 H. Zhang, Z. Wang, L. Wang, T. Li, S. He, L. Li, X. Li, S. Liu, J. Li and S. Li, *RSC Adv.*, 2019, **9**, 35003–35010.